Filament rigidity and connectivity tune the deformation modes of active biopolymer networks

Samantha Stam[a,b], Simon L. Freedman[c,d], Shiladitya Banerjee[c,e,f], Kimberly L. Weirich[c], Aaron R. Dinner[b,c,g], and Margaret L. Gardel[b,c,d,1]

[a]Biophysical Sciences Graduate Program, University of Chicago, Chicago, IL 60637; [b]Institute for Biophysical Dynamics, University of Chicago, Chicago, IL 60637; [c]James Franck Institute, University of Chicago, Chicago, IL 60637; [d]Department of Physics, University of Chicago, Chicago, IL 60637; [e]Department of Physics and Astronomy, University College London, London WC1E 6BT, United Kingdom; [f]Institute for Physics of Living Systems, University College London, London WC1E 6BT, United Kingdom; and [g]Department of Chemistry, University of Chicago, Chicago, IL 60637

Molecular motors embedded within collections of actin and micro-tubule filaments underlie the dynamics of cytoskeletal assemblies. Understanding the physics of such motor-filament materials is critical to developing a physical model of the cytoskeleton and designing biomimetic active materials. Here, we demonstrate through experiments and simulations that the rigidity and connectivity of filaments in active biopolymer networks regulates the anisotropy and the length scale of the underlying deformations, yielding materials with variable contractility. We find that semiflexible filaments can be compressed and bent by motor stresses, yielding materials that undergo predominantly biaxial deformations. By contrast, rigid filament bundles slide without bending under motor stress, yielding materials that undergo predominantly uniaxial deformations. Networks dominated by biaxial deformations are robustly contractile over a wide range of connectivities, while networks dominated by uniaxial deformations can be tuned from extensile to contractile through cross-linking. These results identify physical parameters that control the forces generated within motor-filament arrays and provide insight into the self-organization and mechanics of cytoskeletal assemblies.

actin | myosin | active matter | mechanics | agent-based simulation

Assemblies of semiflexible filaments and molecular motors are active materials (1) that drive many physiological processes such as muscle contraction (2), cytokinesis (3), cytoplasmic transport (4), and chromosome segregation (5). To actuate these processes, the nanometer-scale displacements of motors and local deformation and sliding of filaments must give rise to coordinated mesoscale deformations. These mesoscale dynamics result in the transmission of cellular-scale forces with different directions (e.g., contractile or extensile) and shapes (e.g., isotropic or anisotropic) which result in shape changes at cellular and tissue length scales. Characterizing deformations in active networks of different molecular compositions is a much-needed step toward understanding complex force transmission and shape changes observed in cells and tissues.

Understanding how assemblies of filaments and motors produce a net contractile or extensile force has been extensively explored theoretically (6–14). Testing these models experimentally has been challenging due to variability in protein composition from one system to another and limitations in the ability to systematically alter physical properties. In vitro networks constructed from actin filaments and myosin II motors are robustly contractile (15–18). By contrast, systems of microtubules and molecular motors are either extensile (6, 7, 19–21) or contractile (21–23). One difference between these two active materials is that microtubules are significantly more rigid than actin filaments. Recent work has shown that contractile stress can be generated via motor stress-induced filament buckling (11–14, 17), indicating an important role for filament rigidity. Alternative microscopic mechanisms to generate extensile or contractile stress by motor-mediated sliding of rigid filaments have also been proposed (6–10, 13, 21).

Deformations within active matter can be characterized beyond whether they are contractile or extensile. For example, network-scale force transmission is affected by network connectivity, which regulates the length scale of contraction (15, 16, 24–26). Moreover, recent data suggest that disordered actomyosin networks contract isotropically, indicating the importance of deformation shape (27, 28). By contrast, in vivo, anisotropic contraction dominates cell division and muscle contraction (29). Understanding how to control the deformation anisotropy will further our understanding of how contractile deformations are regulated in vivo.

Here, we directly vary the stiffness and connectivity of filaments within an in vitro biopolymer network through cross-linking and investigate the effects on network deformation. Through quantitative analysis of experimental data we determine that these mechanical changes influence the anisotropy and contractility of deformations caused by the motor protein myosin II. Networks composed of semiflexible filaments that can be buckled by motor stresses exhibit robust biaxial contraction. Increasing the filament rigidity results in uniaxial deformation, the contractility of which is regulated by cross-linker density. Extensile deformations are generated at low cross-linker density and contractile deformations occur at high cross-linker density. Using corresponding agent-based simulations we identify the microscopic deformation modes driving these mesoscale rearrangements. In particular, we find that contractile forces in networks of rigid filaments are transmitted uniaxially by filament sliding. Together, our results indicate how

Significance

Living cells spontaneously change their shape in physiological processes like cell migration and division. Forces generated by molecular motors on biopolymers must underlie these dynamics, but how molecular-scale forces give rise to cellular-scale shape changes is unknown. We use experimental measurements on reconstituted actomyosin networks and computer simulations to show that polymer stiffness and connectivity regulate motor-generated stresses and, in turn, longer-length-scale shape deformations. Importantly, we find that filament rigidity controls whether stresses transmitted are uniaxial or biaxial and that, for rigid filaments, the connectivity can control a transition between extensile and contractile deformations. These results have implications for how conserved molecular mechanisms give rise to diverse morphogenic events in cells.

motor-filament interactions can generate forces that result in either extensile or contractile deformations, which vary in shape depending on the filament rigidity and connectivity. From our experimental and simulation data, we propose a phase diagram of active matter constructed from motors and filaments.

Results

Networks of Cross-Linked Rigid Bundles Are Contractile with a Short Correlation Length. To investigate the role of filament rigidity in active motor-filament networks we construct a quasi-2D layer of actin in vitro by polymerization of 1 µM monomeric actin in the presence of a depletion agent to crowd actin filaments near a passivated surface (17, 19) (Fig. 1A). To increase filament rigidity, we add 0.1 µM of the actin cross-linker fascin, which constructs bundles of ~8 ± 7 actin filaments (Fig. S1). Actin filaments are polar, and their barbed ends are uniformly directed within fascin bundles (30). Fascin bundles, then, maintain the polarity of single actin filaments but are much more rigid (Fig. 1B): The persistence length of bundles is estimated to be ~250 µm (31), over 10 times that of a single actin filament (32). Although actin bundling potentially could affect the interactions between actin and myosin, the myosin filaments in our experiments move along the fascin bundles unidirectionally with an average velocity of ~2.5 µm/s (*Materials and Methods*), which is close to the unloaded gliding speed of skeletal muscle myosin II (33, 34). To connect rigid bundles into networks, we add a small amount (0.002 µM) of a second cross-linker, filamin. Filamin is a large (200 nm) and flexible cross-linker that binds overlapping bundles with varying orientations into a quasi-2D network (35, 36).

After assembling actin filaments or bundles, we add myosin II and monitor structural changes in the actin networks via fluorescence microscopy (*Materials and Methods*). Myosin II filaments (white puncta) initially accumulate on the networks, and we define the time of the maximum density of myosin puncta as $t = 0$ s (Fig. S2). Myosin drives changes in actin filament or bundle orientation, position, and shape that ultimately result in the formation of actomyosin asters composed of polarity-sorted actin filaments oriented radially with large myosin foci at the center (Fig. 1 C and D and Fig. S2 and Movies S1 and S2).

To assess the network motion leading to aster formation we calculate local displacement vectors of the actin network between frames using particle image velocimetry (PIV) (*Materials and Methods* and Fig. 1E). To visualize propagation of contractile or extensile motion we calculate the moment of the velocity field, $\vec{v}_{act}(\vec{r}) \cdot \vec{r}$, where $\vec{v}_{act}(\vec{r})$ is the local actin PIV vector and $\vec{r}$ is
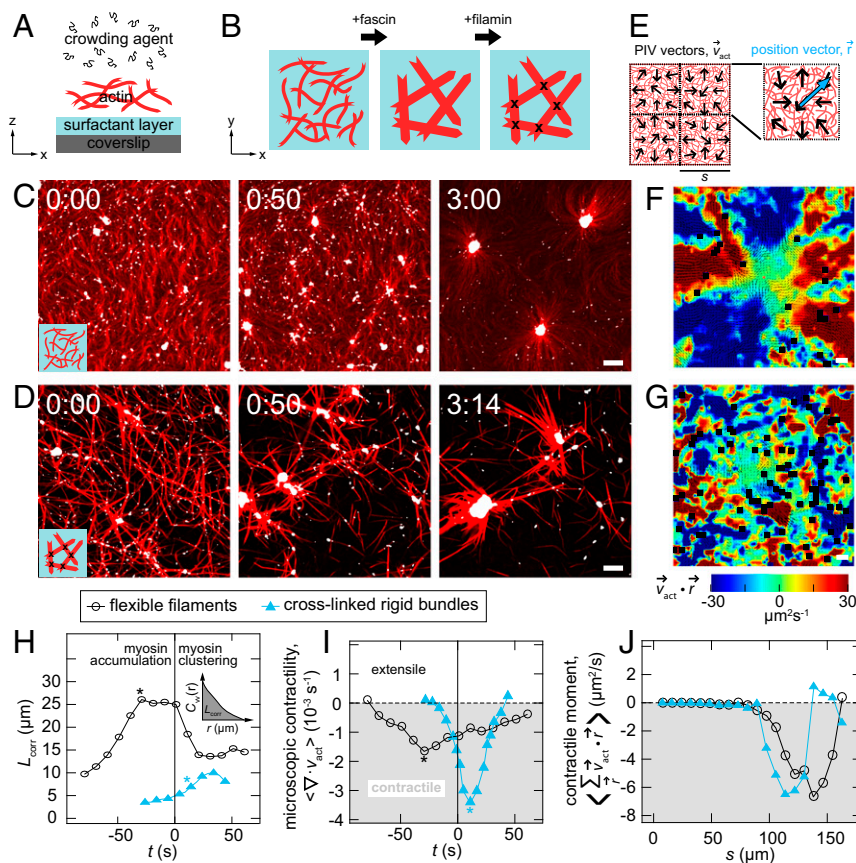

Fig. 1. Networks of cross-linked rigid bundles are contractile with a short correlation length. (A) Schematic of experimental setup. Actin filaments are crowded to a surfactant-coated coverslip surface to make a dense quasi-2D layer. (B) Fascin is used to make rigid, unipolar actin bundles. Filamin is used to cross-link bundles. (C) Images of semiflexible filaments (red) in the absence of fascin or filamin after the addition of myosin (white puncta). (D) Images of cross-linked rigid bundles formed by F-actin in the presence of fascin (1:10) and filamin (1:500) after myosin is added. (E) PIV detects local motion of F-actin ($\vec{v}_{act}$, black arrows). Images are split into boxes of size s, and $\vec{r}$ defines a vector from the center of a box to a PIV vector within the box. (F and G) Example spatial maps of the moment of the velocity field for images at −0:40 and 0:00 of C and D, respectively. Negative values of $\vec{v}_{act} \cdot r$ indicate contraction whereas positive values indicate extension. Black areas indicate regions not analyzed due to voids in vector fields. (H) The correlation length as a function of time for single filaments (open black circles) and cross-linked rigid bundles (closed blue triangles). (*Inset*) Schematic indicating how correlation length is obtained from velocity-velocity correlation. (I) The divergence for both networks as a function of time. The asterisks in H and I indicate the time of minimal divergence, as indicated in I. (J) The contractile moment as a function of length scale s for both samples. Time stamps are in the minutes:seconds format where 0:00 indicates the time of the maximal myosin puncta density after the initial increase when myosin is added to the sample and before the decrease due to myosin clustering, as shown in Fig. S2A. (Scale bars in C−G: 10 µm.)

the vector from the center of a square region to the location of the PIV vector (37) (Fig. 1E). Locations where the moment is positive indicate local expansion from the center of the field of view, whereas negative values indicate local compression. During the early stages of network reorganization before aster formation we find that spatial propagation of inwardly or outwardly directed motion is very different in networks of semiflexible filaments and those of cross-linked rigid bundles (Fig. 1 F and G). In networks of semiflexible filaments, motion is highly spatially correlated, with large areas contracting toward the center of the square region in the vertical direction (blue, Fig. 1F) and material moving outward in the horizontal direction (red, Fig. 1F). In contrast, in the bundled network, motion is restricted to smaller, irregularly shaped, interspersed contractile and extensile regions (Fig. 1G).

To characterize the length scale of correlations in the velocity field we consider the velocity–velocity correlation function:

$$C_{vv}(r) = \frac{\langle \vec{v}_{act}(0) \cdot \vec{v}_{act}(r) \rangle}{\langle |\vec{v}_{act}(0)|^2 \rangle},$$

where r is the distance between two velocity vectors $\vec{v}_{act}$. We define a characteristic correlation length, L_{corr}, as the area under the curve of $C_{vv}(r)$ at a given time (Fig. 1H, Inset). In both networks, L_{corr} initially increases as myosin forces accumulate in the network (Fig. 1H). Eventually, L_{corr} decreases as the networks break into clusters. Although L_{corr} has similar trends for both networks, its value is consistently less for the rigid bundle network than for the network of semiflexible filaments. This is consistent with the spatial heterogeneity in the moment of the velocity field observed in the network of rigid bundles, compared with that formed with semiflexible filaments (Fig. 1 F and G).

Next, we assess net contractility using two different metrics. The divergence of $\vec{v}_{act}$, $\nabla \cdot \vec{v}_{act}$, is a measure of contractility on the
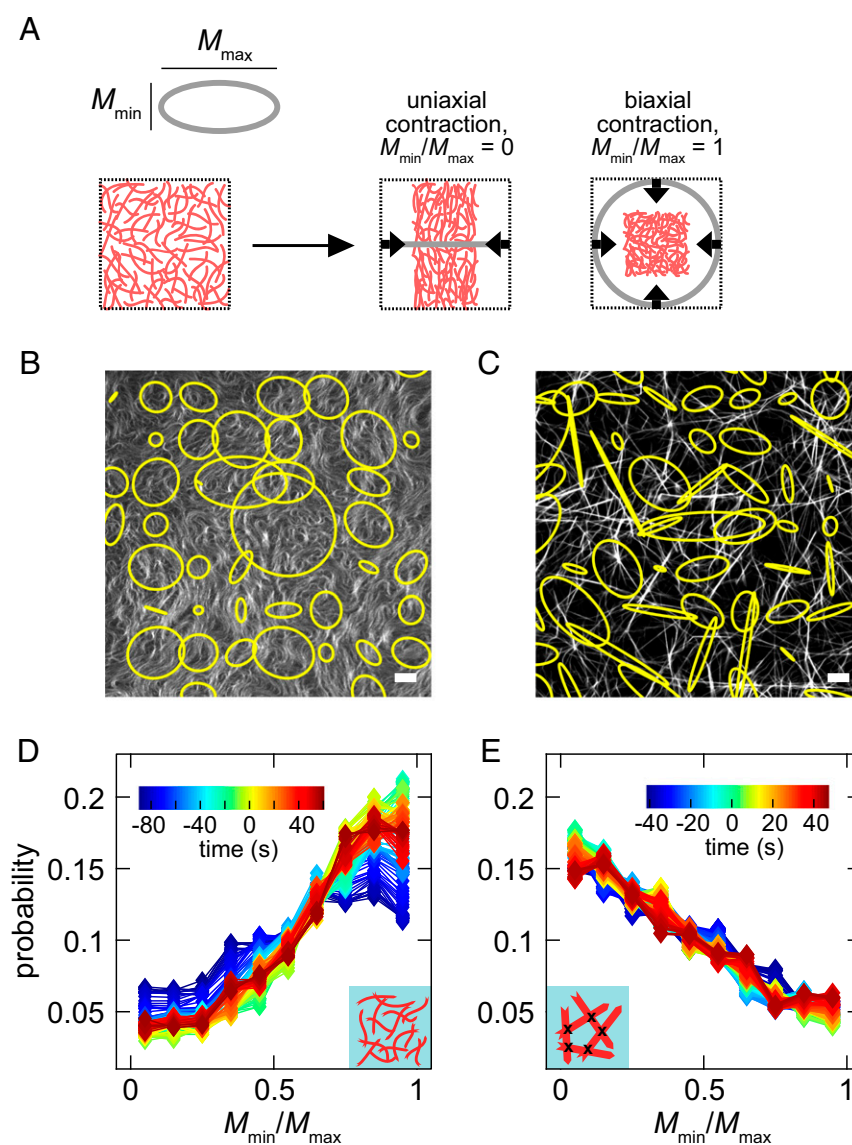

Fig. 2. Deformations are highly biaxial and uniaxial in networks of semiflexible filaments and rigid bundles, respectively. (A) The eigenvalues of the flow dipole moment tensor, M_{min} and M_{max}, are the axes of an ellipse that characterizes the deformation anisotropy, with uniaxial and biaxial contraction illustrated. (B and C) Images of deformation anisotropy in networks of semiflexible filaments (B) and rigid bundles (C). (D and E) Distribution of M_{min}/M_{max} at varying times (color scale) at $s = 20 \, \mu m$ for semiflexible filaments (D) and cross-linked rigid bundles (E). Normalization is such that the 10 points (diamonds) defining each curve sum to 1. (Scale bars in B and C: 10 μm.)

length scale set by the spacing of PIV vectors, in this case 2.4 μm (38). Negative values indicate local contraction while positive values indicate local expansion. For networks of semiflexible filaments, the spatial average of $\nabla \cdot \vec{v}_{act}$ is negative (Fig. 1I, open black circles), indicating net contraction, consistent with previous reports (38). The divergence reaches a maximally negative value as myosin accumulates on the network before separation of actin into clusters, at which point local extension between clusters balances contractility to produce $\langle \nabla \cdot \vec{v}_{act} \rangle \sim 0$ s^{-1}. Similarly, the cross-linked rigid bundle network exhibits a negative divergence that returns to values near 0 s^{-1} after the onset of network coarsening at 0 s (Fig. 1I, filled blue triangles). Thus, the contractility is slightly enhanced in networks of rigid bundles compared with those of semiflexible filaments.

To characterize the length scale of contraction, we measure the contractile moment by summing $\vec{v}_{act}(\vec{r}) \cdot \vec{r}$ (37) over non-overlapping square regions of varying side length s (Fig. 1J). Negative values of the contractile moment indicate that contractile motion propagates across regions with this length scale (37). In both networks, $\langle \sum_{\vec{r}} \vec{v}_{act}(\vec{r}) \cdot \vec{r} \rangle$ reaches a minimum for regions of length 100 μm $< s <$ 150 μm. Thus, contraction in both materials can propagate over large length scales. However, the collective motions in the rigid networks consistently occur over shorter length and time scales.

Rigidity Controls the Anisotropy of Contractile Deformations. To explore the origin of the differing spatial distributions of motion within these contractile networks we sought to characterize the local deformations. We apply a method previously used to characterize the anisotropy of forces exerted by cells (37). We consider the tensor

$$M_{ij} = \sum_{\vec{r}} v_{act}(\vec{r})_i r_j,$$

where i and j denote the in-plane spatial coordinates. By diagonalizing this tensor we can extract the principle deformation axes.

The magnitudes of the eigenvalues, M_{max} and M_{min} are the major and minor axes, respectively, of an ellipse characterizing the anisotropy of the deformation (Fig. 2A). A value of M_{min}/M_{max} of 0 indicates a completely uniaxial deformation, while a value of $M_{min}/M_{max} = 1$ indicates a completely biaxial deformation (Fig. 2A). For a given length scale ($s = 20$ μm), a distribution of M_{min}/M_{max} from deformations across the field of view is obtained at each time point (Fig. 2 B and C). In networks of semiflexible filaments, the distribution is clearly weighted toward biaxial deformations ($M_{min}/M_{max} > 0.5$) at all times during contraction (Fig. 2D). By contrast, in cross-linked rigid bundle networks the distribution is highly weighted toward uniaxial deformations ($M_{min}/M_{max} < 0.5$) at all times (Fig. 2E). We find that these characteristic differences in deformation anisotropy between rigid and semiflexible networks persist across length scales varying from $s = 6$ μm up to 60 μm (Fig. S3).

To examine the effect of different deformations on correlated motion and contraction we next consider the change in the fraction of predominantly biaxial ($M_{min}/M_{max} > 0.5$) or uniaxial ($M_{min}/M_{max} < 0.5$) deformations and term these $P_{biaxial}(s)$ and $P_{uniaxial}(s) = 1 - P_{biaxial}(s)$, respectively (Fig. S4). We compare these quantities to the correlation length, L_{corr}, and the microscopic contractility as a function of time. Versions of these quantities that are rescaled to range from 0 to 1 are indicated by lowercase letters, for example $p_{biaxial}(s)$ and l_{corr} (Materials and Methods). For both rigidities, either $p_{biaxial}(s)$ or $p_{uniaxial}(s)$ is positively correlated with l_{corr} and is optimized for a given length scale s (Materials and Methods and Fig. S4). In networks of semiflexible filaments, $p_{biaxial}$ is positively correlated with l_{corr} during network contraction (Fig. 3A). In contrast, for the cross-linked rigid bundle networks, $p_{uniaxial}$ is strongly positively correlated with l_{corr} (Fig. 3B and Fig. S4B).

These data demonstrate that contractility can occur in networks composed of either semiflexible or rigid filaments, consistent with previous reports of contractility in various cross-linked biopolymer networks (15–18, 21). Our analysis reveals significant differences, however, in the mesoscale shape changes induced within the two networks, with compliant networks supporting biaxial contraction and rigid networks supporting uniaxial deformations.
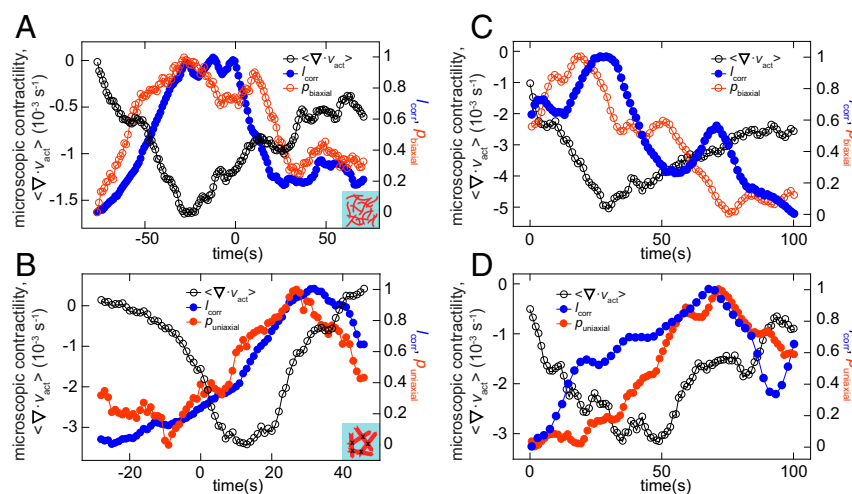

Fig. 3. Activation of biaxial or uniaxial deformations in semiflexible filament and rigid bundle networks, respectively, coincides with correlated motion and contractility. Plot of the divergence (open black circles), correlation length (filled blue circles) and either biaxial probability (A, filled red circles) or uniaxial probability (B, filled red circles) as a function of time for single filaments (A) and cross-linked rigid bundles (B). The length scale chosen to calculate biaxial or uniaxial probability is determined to be the optimal one, as shown in Fig. S4 and is $s = 25$–30 μm in A and 55–60 μm in B. (C and D) Analogs of A and B for simulated networks. In C $L_p = 2.5$ μm and in D $L_p = 250$ μm. The length scale for both biaxial and uniaxial probabilities is $s = 20$ μm. In the experimental data of A and B, $t = 0$ s indicates the time of maximal myosin puncta density after the initial increase when myosin is added to the sample and before the decrease due to myosin clustering, as shown in Fig. S2A. In C and D, $t = 0$ s indicates the beginning of the simulations.

To determine whether a change in filament stiffness is sufficient to alter deformation we use agent-based simulations (39) (*Materials and Methods*). In brief, we model actin filaments as worm-like chains and model cross-linkers and motors as linear springs with two sites (heads) that can attach and detach to the filaments via a Monte Carlo procedure. When attached, motor heads walk toward filament barbed ends at a load-dependent speed. We use Langevin dynamics to evolve each mechanical component of the assembly in response to internal forces. When parameterized as detailed in ref. 39 this model captures a variety of experimentally observed trends with reasonable quantitative accuracy. We implicitly model bundling, corresponding to experimental fascin-bundled actin, by varying the persistence length of the actin filament (L_p). We explicitly model cross-linking, corresponding to the experimental cross-linker filamin, by a spring with rest length 0.15 μm and stiffness 1 pN/μm (36). Myosin minifilaments are modeled similarly, as springs with rest length 0.5 μm, unloaded speed $v_0 = 1$ μm/s, and stall force 10 pN.

Consistent with experiments, we observe that motors (white rectangles) move actin filaments and rearrange the filaments into asters (Fig. 4 *A* and *B* and Movies S5 and S6). The microscopic contractility, $\nabla \cdot \vec{v}_{act}$, decreases to negative values and subsequently increases as the networks form asters and contraction stops (Fig. 3 *C* and *D*, black circles). The trends in $p_{biaxial}$ (Fig. 3*C*, red circles and Fig. S5*A*), $p_{uniaxial}$ (Fig. 3*D*, red circles and Fig. S5*B*), and l_{corr} (Fig. 3 *C* and *D*, blue circles) are similar to the experimental results as well. The quantitative differences between the computational and experimental results likely derive from the fact that the size of the simulation region necessitates a smaller value of L_p in the simulation ($L_p = 2.5$ μm, compared with $L_p = 17$ μm for actin) and s in the computational analysis ($s = 20$ μm, compared with $s = 25$–30 μm in Fig. 3*A* and 55–60 μm in Fig. 3*B*).

Uniaxial Contraction Arises from Filament Sliding Arrested by Cross-Linker Accumulation. We perform simulations over a range of filament rigidities (2.5–250 μm) and cross-linker densities (0–1 μm^{-2}).
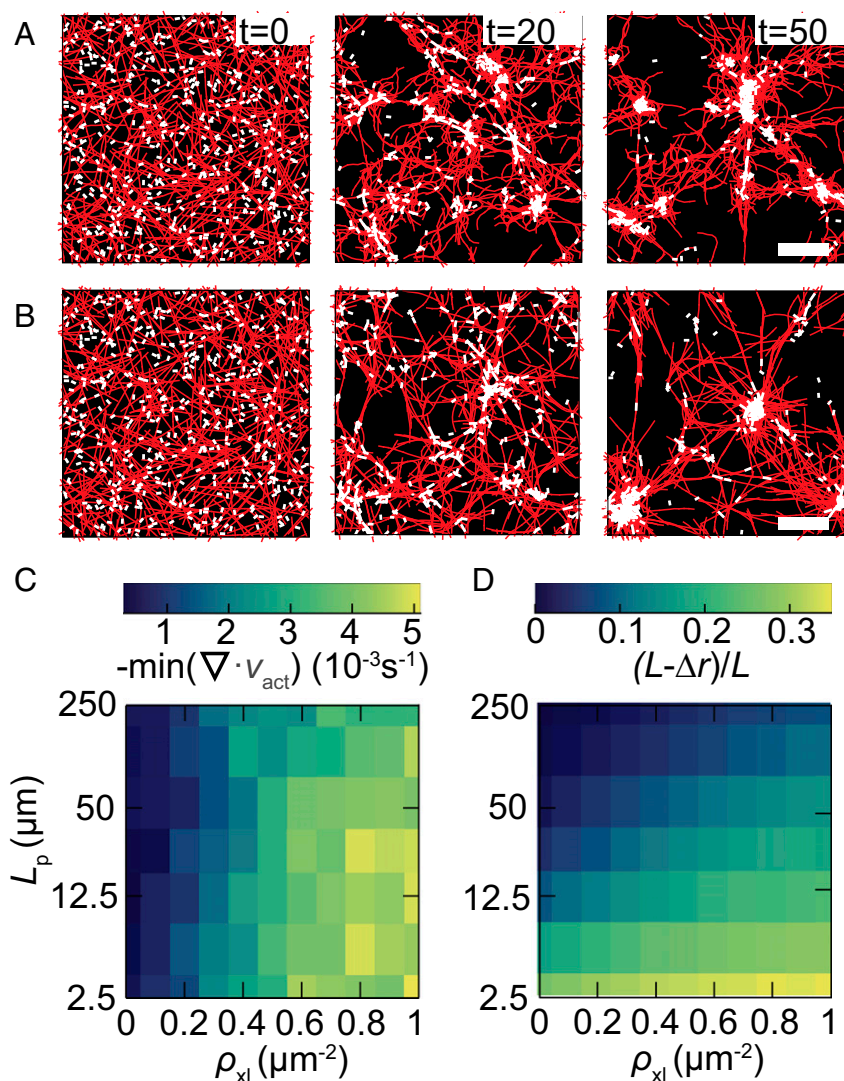

Fig. 4. Simulations indicate cross-link dependent contractility over a wide range of filament stiffness. (*A* and *B*) Time series images in simulations for networks with lower filament stiffness ($L_p = 12.5$ μm, *A*) and higher filament stiffness ($L_p = 250$ μm, *B*). Actin is shown in red and myosin is white. (Scale bars: 10 μm.) Times (t) indicated in seconds. (*C*) Microscopic contractility at varying filament stiffness and cross-linker density (ρ_{xl}), measured by the minimum of the spatially averaged divergence of the actin velocity field in the first 25 s of simulation. (*D*) Filament compression during the first 25 s of simulation as a function of stiffness and cross-linker density.
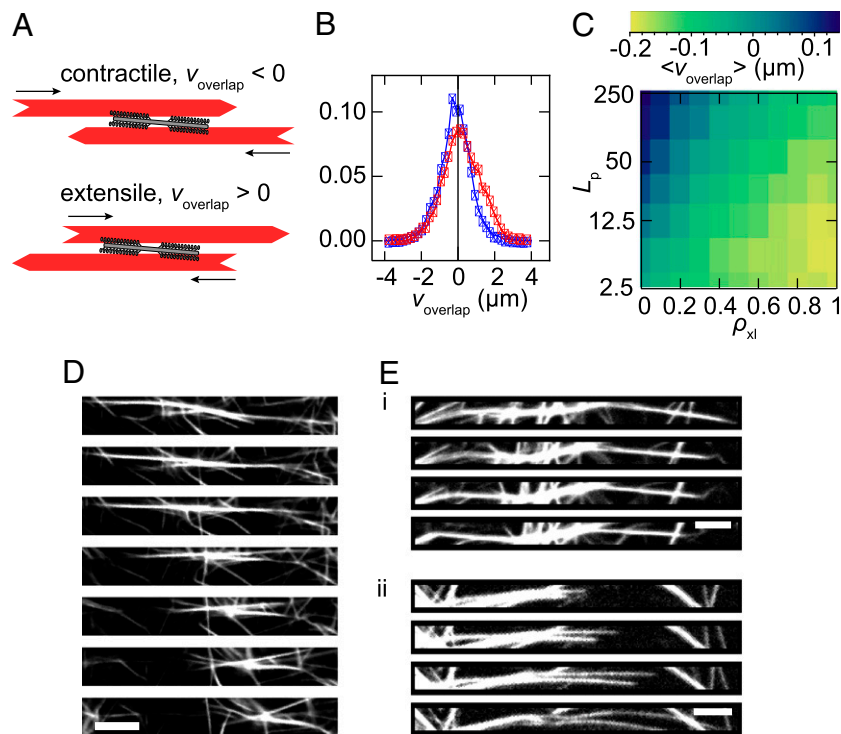
Fig. 5. Uniaxial contractility is caused by arrested filament sliding. (*A*) A pair of antiparallel filaments are contractile if the myosin is near the pointed ends (*Top*) and extensile if myosin is proximal to the barbed ends (*Bottom*). (*B*) The distribution of $v_{overlap}$ is shifted to more extensile values for rigid ($L_p = 250$ µm) filaments without cross-linking (red squares) compared with the same filaments with $\rho_{xl} = 1$ µm^{-2} (blue squares). This distribution is from the first 10 s of simulation. (*C*) Average of $v_{overlap}$ over 25 s of simulation with varying filament rigidity and cross-linker density. (*D*) In experiments with cross-linked rigid bundles, the bundles are observed to slide together and become arrested in the contracted state. The time delay between images from top to bottom is 1 s. (*E*) In the absence of filamin, myosin drives both contractile (*i*) and extensile (*ii*) motions of rigid bundle pairs. The time delay between frames from top to bottom in both *i* and *ii* is 1 s. (Scale bars in *D* and *E*: 5 µm.)

These simulations reveal that microscopic contractility is generally more sensitive to changes in cross-linker density than filament rigidity (Fig. 4*C*). This result is surprising, as we previously iden-tified filament buckling as the microscopic mechanism underlying contractility in networks of actin and myosin (17). To check whether this mechanism is operative in the simulations we quantify
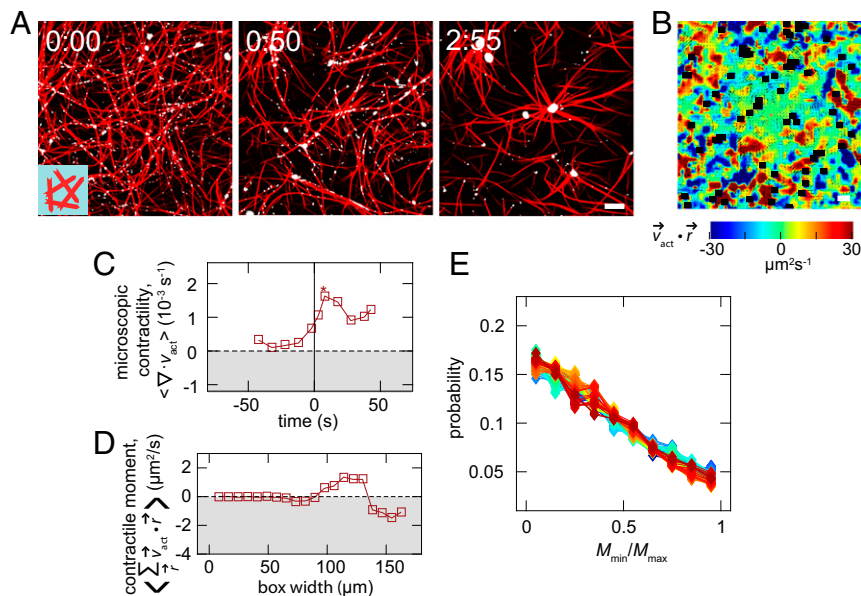

Fig. 6. Myosin reorganizes rigid bundles lacking filamin cross-links via uniaxial forces. (*A*) Image sequence of fascin bundles without filamin. Actin is shown in red and myosin in white. (*B*) Values of $\vec{v}_{act} \cdot \vec{r}$ over a (150 µm)^2 square region. Black areas indicate regions not analyzed due to voids in vector fields. (*C*) The divergence of $\vec{v}_{act}$ is noncontractile over the course of network rearrangement. (*D*) The contractile moment, $\langle \sum_{\vec{r}} \vec{v}_{act} \cdot \vec{r} \rangle$, calculated over a 30-s interval after the maximum divergence in *C*. (*E*) Distribution of M_{min}/M_{max}, $s = 20$ µm, indicates that deformations are predominantly uniaxial. (Scale bars in *A* and *B*: 10 µm.)

filament compression, $(L - \Delta r)/L$, where L is the filament contour length and Δr is the end-to-end distance. This measure is zero when filaments are perfectly straight ($\Delta r = L$) and greater than zero if they are bent. As expected, buckling is prevalent at low filament rigidity (Fig. 4D). Here, we note that the shift to increasingly biaxial deformations in the experimental distribution of M_{min}/M_{max} (Fig. S3A) occurs concurrently with the development of visible buckling and bending in filaments, indicating that buckling is the underlying cause of biaxial contraction (Movie S3). This shift does not happen in the network of cross-linked rigid bundles (Movie S4), because buckling is suppressed by the increased filament rigidity. Consistent with this observation, there is a sizable region of the simulation parameter space over which contractility occurs in the absence of filament compression (Fig. 4 C and D).

An alternate microscopic mechanism that could account for the contractility at higher rigidities is myosin-driven actin sliding (6, 8, 9, 13, 21). Actin sliding drives local contraction when a motor connected to two antiparallel filaments is closer to their pointed ends and local extension when it is closer to their barbed ends (Fig. 5A). In the absence of symmetry-breaking mechanisms, this results in no net force propagation as extensile and contractile deformations balance. However, when filaments overlap there are more sites for cross-linkers to bind bivalently. This suppresses extensile motions that propagate force into the surrounding network (6, 21).

We examine the probability distribution of relative sliding velocity, $v_{overlap}$, in simulations of rigid ($L_p = 250$ μm) filaments both with ($\rho_{xl} = 1$ μm^{-2}) and without cross-linkers. The distribution of overlap velocities shifts to negative values with the addition of cross-linkers (Fig. 5B). By examining the relative sliding velocity across all parameter values, we observe that the system is contractile ($\langle v_{overlap} \rangle < 0$) over most rigidities and cross-linker densities (Fig. 5C). However, at the lowest cross-linker densities and highest filament rigidities we observe a regime where $\langle v_{overlap} \rangle > 0$, indicating that extensile motions dominate, consistent with theory (6, 7, 21).

To seek experimental evidence for extensile sliding we examined pairs of bundles undergoing relative sliding. Indeed, in the presence of cross-linkers (1:500 filamin:actin) we observe bundle pairs sliding relative to each other, increasing the overlap, and then stopping (Fig. 5D). In a network without cross-linkers we see both bundles that increase their overlap (Fig. 5 E, i) and that extend further apart (Fig. 5 E, ii). The latter is similar to extensile motions observed in active liquid crystals of microtubules and kinesin (20) but leads to the formation of asters (40, 41). Thus, our simulations and experiments of rigid filaments suggest that cross-linker density can control the transition from contractile to extensile deformations, consistent with recent publications (6, 21, 26).

Motors Drive Aster Formation Within Networks of Rigid Bundles Without Cross-Links via Uniaxial, Extensile Forces. To understand the consequences of the microscopic extensile deformations described above we study the myosin-driven reorganization of rigid actin bundles that lack filamin cross-linkers but are sufficiently dense to have numerous overlaps such that myosin motors can slide and rearrange bundles to eventually form asters (Fig. 6A and Movie S7). Asters are composed of a dense myosin cluster with polarity-sorted actin bundles emanating from the center, similar to those previously described (Fig. 6A and Fig. S2). The spatial map of the moment of the velocity field reveals small, interspersed, contractile and extensile regions (Fig. 6B) with short velocity–velocity correlation lengths (Fig. S6). Consistent with simulations (Fig. 5C), the divergence of the velocity field indicates net extensile deformation (Fig. 6C) and the contractile moment is weakly positive at ~100 μm
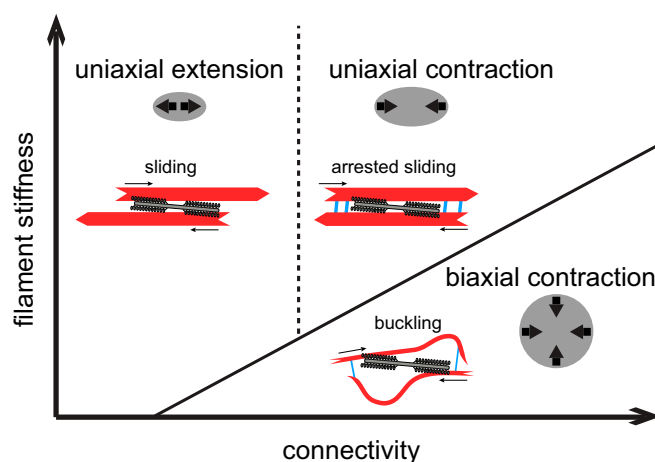

Fig. 7. Uniaxial and biaxial deformations indicate differences in the mechanism of contractility and force propagation. Starting from the top left of the diagram, the three states we observe are uniaxial extension, uniaxial contraction, and biaxial contraction. The shape of the boundaries between these mechanisms are based on the simulation phase diagrams in Figs. 4D and 5C. The mechanisms can be identified by the characteristic anisotropy of the transmitted strain, which is predominantly uniaxial for sliding and biaxial for buckling.

(Fig. 6D). Although the minimum divergence of the velocity field is weakly negative if the PIV vectors are calculated at sufficiently large time delays and length scales, the divergence values are always less negative than in the other two networks (Fig. S7). Consistent with motions dominated by filament sliding, deformations are predominantly uniaxial (Fig. 6E and Fig. S3C and Movie S8). Thus, actin sliding is responsible for short-range extensile, uniaxial deformations that drive local rearrangement of actin bundles into polarity-sorted asters.

Discussion

Our work demonstrates how local shape deformations within active biopolymer networks can be altered by modifications to filament rigidity and cross-link density. Changes to these biophysical parameters alter the microscopic mechanisms of active stress and subsequent structural rearrangements. Using this information we map three phases of deformations that are characterized by their anisotropy, length scale, and contractility. The different phases are elicited by modifying filament rigidity and connectivity (Fig. 7). Each phase is consistent with network conditions favoring one of three microscopic deformation modes: filament buckling, filament sliding, or arrested filament sliding. We show that buckling results in predominantly biaxial deformation modes, whereas sliding results in predominantly uniaxial deformation modes. These results have implications for how the various physical properties of cytoskeletal networks support different deformations and how cells or tissues change shape when the resulting forces are propagated to larger length scales. Such control over the shape of the deformations could be used to sculpt active materials both in vitro and in vivo.

We are now in a position to formulate a framework (Fig. 7) that can unify previous observations of both extensile and contractile behaviors in active microtubule systems (6, 7, 19–23) with the robust contractility typically observed in actin networks (15–18). Motor-induced filament buckling drives contractility when motor stresses exceed the Euler buckling force of filaments (11–13, 17). For a constant motor density we expect increased connectivity to enable higher stresses (26, 42), while increased rigidity raises the force required for buckling (Fig. 7, solid black line). When buckling is suppressed, motor-mediated sliding of antiparallel

filaments becomes the dominant deformation mode. In this phase, cross-linker density qualitatively changes the motor-mediated deformations of rigid filaments from extensile to contractile (Fig. 7, dashed line). When cross-linkers are absent, enhanced motor binding for highly overlapping filaments favors the generation of extensile stresses (6, 7). When cross-linkers are present, they can bind to highly overlapping filaments and attenuate extensile stresses (6, 21). In future work it will be interesting to explore the transitions between other microscopic deformation modes in active motor-filament systems and see how these are controlled by changes or heterogeneity in the local structure and composition (e.g., filament orientation or polarity organization).

We note that many previous studies (15–18, 22–24, 40, 41, 43–46) have equated the formation of asters in actomyosin networks with contractility. Associated theoretical models have assumed that motors always produce contractile force dipoles (47). However, our analysis shows that similar structures can result from isotropic and anisotropic contractility, as well as anisotropic extension. This underscores the importance of characterizing dynamics rather than relying on final structures alone to elucidate physical mechanisms.

Finally, our analysis strategies may be used for assessing and understanding the underlying physical mechanisms of force propagation in a variety of active biopolymer systems. We modify previous metrics (37) to detect propagation of contraction or extension across varying length scales. We also determine which deformations (biaxial or uniaxial) are responsible for correlated motion. Similar techniques could be used to understand the deformations of motor-filament arrays in the actin and microtubule cytoskeletons during processes including cell migration, cell division, intracellular transport, and formation of the mitotic spindle. Beyond the cytoskeleton, intranuclear molecular motors can drive correlated motion of chromatin (48), and forces produced by whole bacterial or mammalian cells can drive motions such as biofilm contraction or growth (49, 50) or alignment and organization of filamentous extracellular matrices (51–53). The physical properties of deformations that occur during these processes and the mechanisms at the level of biopolymer deformation or translocation have not been explored. Investigations of this nature will reveal which features of active matter dynamics are fundamental across these highly diverse systems and which features are regulated by particular biopolymer and motor network properties.

Materials and Methods

In all experiments, 1 μM actin filaments (F-actin) in the presence of binding proteins fascin or filamin are crowded to a passivated surface with a 0.3% methylcellulose solution for >15 min. All imaging is performed using spinning-disk confocal microscopy and image analysis is peformed in ImageJ or MATLAB. For the simulations, we used AFINES, a software package we developed for modeling active polymer networks. Details of all methods can be found in SI Materials and Methods.

1. Marchetti MC, et al. (2013) Hydrodynamics of soft active matter. *Rev Mod Phys* 85: 1143–1189.
2. Gautel M, Djinović-Carugo K (2016) The sarcomeric cytoskeleton: From molecules to motion. *J Exp Biol* 219:135–145.
3. Fededa JP, Gerlich DW (2012) Molecular control of animal cell cytokinesis. *Nat Cell Biol* 14:440–447.
4. Munro E, Nance J, Priess JR (2004) Cortical flows powered by asymmetrical contraction transport PAR proteins to establish and maintain anterior-posterior polarity in the early C. elegans embryo. *Dev Cell* 7:413–424.
5. Gadde S, Heald R (2004) Mechanisms and molecules of the mitotic spindle. *Curr Biol* 14:R797–R805.
6. Blackwell R, et al. (2016) Microscopic origins of anisotropic active stress in motor-driven nematic liquid crystals. *Soft Matter* 12:2676–2687.
7. Gao T, Blackwell R, Glaser MA, Betterton MD, Shelley MJ (2015) Multiscale polar theory of microtubule and motor-protein assemblies. *Phys Rev Lett* 114:048101.
8. Liverpool TB, Marchetti MC (2005) Bridging the microscopic and the hydrodynamic in active filament solutions. *EPL* 69:846–852.
9. Kruse K, Jülicher F (2000) Actively contracting bundles of polar filaments. *Phys Rev Lett* 85:1778–1781.
10. Dasanayake NL, Michalski PJ, Carlsson AE (2011) General mechanism of actomyosin contractility. *Phys Rev Lett* 107:118101.
11. Liverpool TB, Marchetti MC, Joanny JF, Prost J (2009) Mechanical response of active gels. *EPL* 85:18007.
12. Lenz M, Thoresen T, Gardel ML, Dinner AR (2012) Contractile units in disordered actomyosin bundles arise from F-actin buckling. *Phys Rev Lett* 108:238107.
13. Belmonte JM, Leptin M, Nédélec F (2017) A theory that predicts behaviors of disordered cytoskeletal networks. *Mol Syst Biol* 13:941.
14. Ronceray P, Broedersz CP, Lenz M (2016) Fiber networks amplify active stress. *Proc Natl Acad Sci USA* 113:2827–2832.
15. Janson LW, Kolega J, Taylor DL (1991) Modulation of contraction by gelation/solation in a reconstituted motile model. *J Cell Biol* 114:1005–1015.
16. Alvarado J, Sheinman M, Sharma A, MacKintosh FC, Koenderink GH (2013) Molecular motors robustly drive active gels to a critically connected state. *Nat Phys* 9:591–597.
17. Murrell MP, Gardel ML (2012) F-actin buckling coordinates contractility and severing in a biomimetic actomyosin cortex. *Proc Natl Acad Sci USA* 109:20820–20825.
18. Köhler S, Bausch AR (2012) Contraction mechanisms in composite active actin networks. *PLoS One* 7:e39869.
19. Sanchez T, Chen DT, DeCamp SJ, Heymann M, Dogic Z (2012) Spontaneous motion in hierarchically assembled active matter. *Nature* 491:431–434.
20. Henkin G, DeCamp SJ, Chen DT, Sanchez T, Dogic Z (2014) Tunable dynamics of microtubule-based active isotropic gels. *Philos Trans A Math Phys Eng Sci* 372: 20140142.
21. Stanhope KT, Yadav V, Santangelo CD, Ross JL (2017) Contractility in an extensile system. *Soft Matter* 13:4268–4277.
22. Foster PJ, Fürthauer S, Shelley MJ, Needleman DJ (2015) Active contraction of microtubule networks. *Elife* 4:e10837.
23. Torisawa T, Taniguchi D, Ishihara S, Oiwa K (2016) Spontaneous formation of a globally connected contractile network in a microtubule-motor system. *Biophys J* 111: 373–385.
24. Bendix PM, et al. (2008) A quantitative analysis of contractility in active cytoskeletal protein networks. *Biophys J* 94:3126–3136.
25. Wang S, Wolynes PG (2012) Active contractility in actomyosin networks. *Proc Natl Acad Sci USA* 109:6446–6451.
26. Ennomani H, et al. (2016) Architecture and connectivity govern actin network contractility. *Curr Biol* 26:616–626.
27. Linsmeier I, et al. (2016) Disordered actomyosin networks are sufficient to produce cooperative and telescopic contractility. *Nat Commun* 7:12615.
28. Schuppler M, Keber FC, Kröger M, Bausch AR (2016) Boundaries steer the contraction of active gels. *Nat Commun* 7:13120.
29. Murrell M, Oakes PW, Lenz M, Gardel ML (2015) Forcing cells into shape: The mechanics of actomyosin contractility. *Nat Rev Mol Cell Biol* 16:486–498.
30. Ishikawa R, Sakamoto T, Ando T, Higashi-Fujime S, Kohama K (2003) Polarized actin bundles formed by human fascin-1: Their sliding and disassembly on myosin II and myosin V in vitro. *J Neurochem* 87:676–685.
31. Claessens MM, Bathe M, Frey E, Bausch AR (2006) Actin-binding proteins sensitively mediate F-actin bundle stiffness. *Nat Mater* 5:748–753.
32. Gittes F, Mickey B, Nettleton J, Howard J (1993) Flexural rigidity of microtubules and actin filaments measured from thermal fluctuations in shape. *J Cell Biol* 120:923–934.
33. Spudich JA, Kron SJ, Sheetz MP (1985) Movement of myosin-coated beads on oriented filaments reconstituted from purified actin. *Nature* 315:584–586.
34. Kron SJ, Spudich JA (1986) Fluorescent actin filaments move on myosin fixed to a glass surface. *Proc Natl Acad Sci USA* 83:6272–6276.
35. Hartwig JH, Stossel TP (1979) Cytochalasin B and the structure of actin gels. *J Mol Biol* 134:539–553.
36. Hartwig JH, Stossel TP (1981) Structure of macrophage actin-binding protein molecules in solution and interacting with actin filaments. *J Mol Biol* 145:563–581.
37. Butler JP, Tolić-Nørrelykke IM, Fabry B, Fredberg JJ (2002) Traction fields, moments, and strain energy that cells exert on their surroundings. *Am J Physiol Cell Physiol* 282: C595–C605.
38. Murrell M, Gardel ML (2014) Actomyosin sliding is attenuated in contractile biomimetic cortices. *Mol Biol Cell* 25:1845–1853.
39. Freedman SL, Banerjee S, Hocky GM, Dinner AR (2017) A versatile framework for simulating the dynamic mechanical structure of cytoskeletal networks. *Biophys J* 113: 448–460.
40. Nédélec FJ, Surrey T, Maggs AC, Leibler S (1997) Self-organization of microtubules and motors. *Nature* 389:305–308.

41. Urrutia R, McNiven MA, Albanesi JP, Murphy DB, Kachar B (1991) Purified kinesin promotes vesicle motility and induces active sliding between microtubules in vitro. *Proc Natl Acad Sci USA* 88:6701–6705.

42. Lenz M (2014) Geometrical origins of contractility in disordered actomyosin networks. *Phys Rev X* 4:041002.

43. Köhler S, Schaller V, Bausch AR (2011) Structure formation in active networks. *Nat Mater* 10:462–468.

44. Soares e Silva M, et al. (2011) Active multistage coarsening of actin networks driven by myosin motors. *Proc Natl Acad Sci USA* 108:9408–9413.

45. Backouche F, Haviv L, Groswasser D, Bernheim-Groswasser A (2006) Active gels: Dynamics of patterning and self-organization. *Phys Biol* 3:264–273.

46. Vogel SK, Petrasek Z, Heinemann F, Schwille P (2013) Myosin motors fragment and compact membrane-bound actin filaments. *Elife* 2:e00116.

47. Jülicher F, Kruse K, Prost J, Joanny JF (2007) Active behavior of the cytoskeleton. *Phys Rep* 449:3–28.

48. Zidovska A, Weitz DA, Mitchison TJ (2013) Micron-scale coherence in interphase chromatin dynamics. *Proc Natl Acad Sci USA* 110:15555–15560.

49. Yan J, Sharo AG, Stone HA, Wingreen NS, Bassler BL (2016) Vibrio cholerae biofilm growth program and architecture revealed by single-cell live imaging. *Proc Natl Acad Sci USA* 113:E5337–E5343.

50. Asally M, et al. (2012) Localized cell death focuses mechanical forces during 3D patterning in a biofilm. *Proc Natl Acad Sci USA* 109:18891–18896.

51. Harris AK, Stopak D, Wild P (1981) Fibroblast traction as a mechanism for collagen morphogenesis. *Nature* 290:249–251.

52. Vader D, Kabla A, Weitz D, Mahadevan L (2009) Strain-induced alignment in collagen gels. *PLoS One* 4:e5902.

53. Cetera M, et al. (2014) Epithelial rotation promotes the global alignment of contractile actin bundles during Drosophila egg chamber elongation. *Nat Commun* 5:5511.

54. Spudich JA, Watt S (1971) The regulation of rabbit skeletal muscle contraction. I. Biochemical studies of the interaction of the tropomyosin-troponin complex with actin and the proteolytic fragments of myosin. *J Biol Chem* 246:4866–4871.

55. Margossian SS, Lowey S (1982) Preparation of myosin and its subfragments from rabbit skeletal muscle. *Methods Enzymol* 85:55–71.

56. Verkhovsky AB, Borisy GG (1993) Non-sarcomeric mode of myosin II organization in the fibroblast lamellum. *J Cell Biol* 123:637–652.

57. Craig SW, Lancashire CL, Cooper JA (1982) Preparation of smooth muscle alpha-actinin. *Methods Enzymol* 85:316–321.

58. Vignjevic D, Peloquin J, Borisy GG (2006) In vitro assembly of filopodia-like bundles. *Regulators and Effectors of Small GTPases: Rho Family* (Academic, New York), Vol 406, pp 727–739.

59. Weirich KL, Israelachvili JN, Fygenson DK (2010) Bilayer edges catalyze supported lipid bilayer formation. *Biophys J* 98:85–92.

60. Thévenaz P, Ruttimann UE, Unser M (1998) A pyramid approach to subpixel registration based on intensity. *IEEE Trans Image Process* 7:27–41.

61. Schneider CA, Rasband WS, Eliceiri KW (2012) NIH Image to ImageJ: 25 years of image analysis. *Nat Methods* 9:671–675.